



Article

Nanosized CoO Loaded on Copper Foam for High-Performance, Binder-Free Lithium-Ion Batteries

Mingna Liao ^{1,2}, Qilun Zhang ¹, Fengling Tang ³, Zhiwei Xu ⁴, Xin Zhou ^{1,2}, Youpeng Li ^{1,2}, Yali Zhang ^{1,2}, Chenghao Yang ⁵, Qiang Ru ^{2,*} and Lingzhi Zhao ^{1,2,*}

¹ Institute of Opto-Electronic Materials and Technology, South China Normal University, Guangzhou 510631, China; lmn0769@163.com (M.L.); aaron222222@outlook.com (Q.Z.); zxallin@163.com (X.Z.); youpli@163.com (Y.L.); zhangyalicherish@163.com (Y.Z.)

² Guangdong Provincial Engineering Technology Research Center for Low Carbon and Advanced Energy Materials, Guangzhou 510631, China

³ Department of Medical Engineering, Guangdong Food and Drug Vocational-Technical School, Guangzhou 510663, China; tang15626408613@163.com

⁴ Guangzhou Zhixin Middle School, No.152, Zhixin South Road, Guangzhou 510080, China; lmn0753@163.com

⁵ New Energy Research Institute, School of Environment and Energy, South China University of Technology, Guangzhou 510006, China; esyangc@scut.edu.cn

* Correspondence: ruqiang@scnu.edu.cn (Q.R.); lzzhao@vip.163.com (L.Z.)

Received: 26 January 2018; Accepted: 18 March 2018; Published: 22 March 2018



Abstract: The synthesis of nanosized CoO anodes with unique morphologies via a hydrothermal method is investigated. By adjusting the pH values of reaction solutions, nanoflakes (CoO-NFs) and nanoflowers (CoO-FLs) are successfully located on copper foam. Compared with CoO-FLs, CoO-NFs as anodes for lithium ion batteries present ameliorated lithium storage properties, such as good rate capability, excellent cycling stability, and large reversible capacity. The initial discharge capacity is 1470 mA h g⁻¹, while the reversible capacity is maintained at 1776 mA h g⁻¹ after 80 cycles at a current density of 100 mA h g⁻¹. The excellent electrochemical performance is ascribed to enough free space and enhanced conductivity, which play crucial roles in facilitating electron transport during repetitive Li⁺ intercalation and extraction reaction as well as buffering the volume expansion.

Keywords: CoO nanoflakes; CoO nanoflowers; anodes; binder free; lithium ion batteries

1. Introduction

Over the past few decades, lithium-ion batteries (LIBs) have been widely used as a predominant energy transformation and storage system for laptops, electric vehicles, and portable electronic products [1–3]. Nevertheless, commercial carbonaceous anodes are limited by their low capacity (~372 mA h g⁻¹), which means they can barely meet the growing requirements for next-generation LIBs [4,5]. To solve this problem, a worldwide effort has been made to explore alternative anode materials with higher power density and energy density [6–10]. The transition metal oxides (TMOs) such as tin, nickel, and iron oxides have shown almost three times the capacity of commercial graphite [11–14]. Therefore, CoO has been extensively researched owing to its high theoretical capacities (716 mA h g⁻¹) based on the conversion mechanism and its completely reversible electrochemical reaction as follows: $\text{CoO} + 2\text{Li}^+ + 2\text{e}^- \leftrightarrow \text{Li}_2\text{O} + \text{Co}$, which is different from the reaction of lithium intercalation and de-intercalation in a carbon anode: $6\text{C} + x\text{Li}^+ + xe^- \leftrightarrow \text{Li}_x\text{C}_6$ [15–17]. Nevertheless, the drastic volume expansion effect and poor electrical conductivity restrict the improvement of CoO's electrochemical performance [18–22]. Up to now, a great deal of work has been done to overcome the above issues by designing various

specific nanostructures such as nanospheres [23], nanocubes [24], nanowires [25], nanosheets [26], etc. Although these efforts magnify the interface area of electron/electrolyte and increase reactive sites, they barely promote the electrical conductivity of the electrodes owing to the poor ion/electrical transport kinetics shown by metal oxides [27].

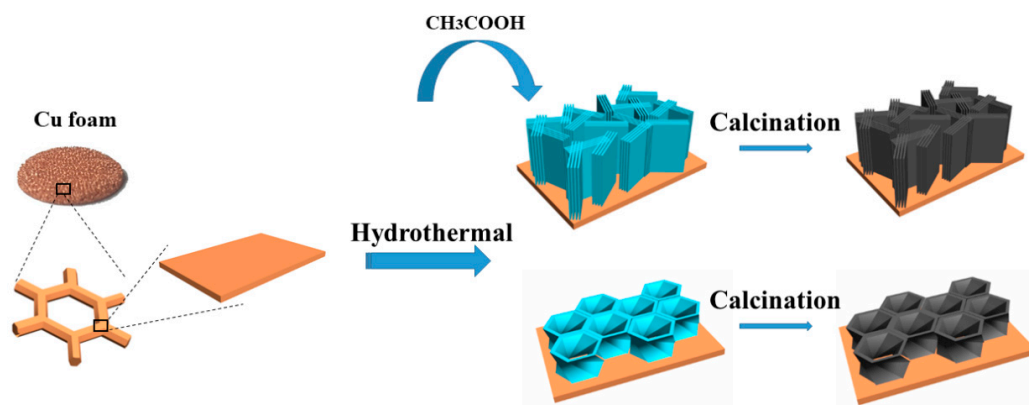
Recently, several research groups have synthesized binder-free anodes by growing various CoO nanostructures directly on the current collector substrate. This is a way to avoid introducing PVDF (Polyvinylidene Fluoride) and carbon black into the anodes. Through this method, no extra weight will be added to the electrodes. What is more, the removal of PVDF can improve the overall electrical conductivity and specific capacity. It has been reported that CoO nanostructures grown on various conductive substrates such as copper foil [28], nickel foam [29], Ti foil [30], and carbon cloth [31]. Huang et al. synthesized the CoO/graphene hybrid on the copper foil by electrostatic interaction and the composite delivered 947 mA h g⁻¹ capacities in the first cycle at 100 mA g⁻¹ [32]. By preparing CoO nanowires on Cu foil through hydrothermal synthesis, Cao et al. fabricated an electrode whose reversible specific capacity could be sustained at 1248.8 mA h g⁻¹ [33]. Zhao et al. used a hydrothermal method to grow hierarchical CoO nanowires on carbon cloth that delivered a reversible capacity of 1300 mA h g⁻¹ at 100 mA g⁻¹ after 90 cycles. However, the capacity of the electrode dropped to 600 mA h g⁻¹ after the current density increased from 100 to 2000 mA g⁻¹ [31]. The above studies made improvements to the electrochemical performance of CoO to some degree; however, there is still room for improvement of the reversible capacity and cycling performance.

In this paper, we fabricated different nanosized CoO by a simple hydrothermal method, including nanoflakes and nanoflowers on copper foam, and directly applied them as anodes for LIBs (shown in Scheme 1). As the temperature rises in the oven, the urea hydrolyzed and released CO₃²⁻ and OH⁻ anions. The formation of a cobalt-hydroxide-carbonate nucleus started, along with the increase in the concentration of anions in the reaction solution. After the annealing process, the precursor was decomposed completely and CoO electrodes were obtained. The overall chemical reactions are expressed as follows: $\text{Co}^{2+} + 0.5(2-x)\text{CO}_3^{2-} + x\text{OH}^- + n\text{H}_2\text{O} \rightarrow \text{Co}(\text{OH})_x(\text{CO}_3)_{0.5(2-x)} \cdot n\text{H}_2\text{O}$; $\text{Co}(\text{OH})_x(\text{CO}_3)_{0.5(2-x)} \cdot n\text{H}_2\text{O} \rightarrow \text{CoO} + 0.5(2-x)\text{CO}_2 + (n+x/2)\text{H}_2\text{O}$. As expected, both CoO-NFs and CoO-FLs displayed a superior rate capability and high reversibility capacity. A comparison of the performance of CoO-NFs in this work and the reported CoO anodes with different morphologies is shown in Table 1.

Table 1. Results reported in the literature on the electrochemical performance of CoO anodes.

Materials		Performance		Reference
CoO	nanoflakes	1776 mA h g ⁻¹ after 80 cycles	At 100 mA g ⁻¹	This work
CoO	nanowire clusters	1249 mA h g ⁻¹ after 50 cycles	At 200 mA g ⁻¹	[33]
CoO	nanowire arrays	1300 mA h g ⁻¹ after 90 cycles	At 100 mA g ⁻¹	[31]
CoO	nanosheet arrays	1000 mA h g ⁻¹ after 100 cycles	At 1000 mA g ⁻¹	[34]
CoO	semisphere arrays	695 mA h g ⁻¹ after 150 cycles	At 500 mA g ⁻¹	[35]
CoO	Cu-doped	800 mA h g ⁻¹ after 80 cycles	At 500 mA g ⁻¹	[17]
CoO	nanosheets	637 mA h g ⁻¹ after 200 cycles	At 100 mA g ⁻¹	[28]

The considerable improvement in performance is mainly owing to the following factors. Firstly, the unique morphologies provide good strain accommodation for the significant volume change of CoO within the Li⁺ extraction and insertion process. Secondly, the uniform and thin CoO growing in situ on copper foam can shorten the charge transfer pathways, causing a faster electronic diffusion. Thirdly, copper foam as a current collector can avoid the adverse influence of PVDF binder with poor electrical conductivity. Moreover, there are rare reports on synthesizing nanosized CoO directly on copper foam through a facile hydrothermal route.



Scheme 1. Schematic illustration of the synthesis process of CoO with two different morphologies on copper foam substrates.

2. Experimental

2.1. Material Preparations

In this work, all the analytical purity reagents were used without further purification. The copper foam, cut into a circular shape 14 mm in diameter, was washed by sonication sequentially in diluted acid solution, acetone, and ethanol separately for 10 min. Typically, 30 mL deionized water were used to dissolve 0.2343 g $\text{CH}_3\text{COOCu}\cdot 4\text{H}_2\text{O}$ and 0.5727 g urea at room temperature under magnetic stirring. The pH value of the mixture was adjusted to 4 by adding ~ 0.2 mL 3 mol/L CH_3COOH solution with 30 min stirring to produce a uniform solution. Then the prepared copper foam was immersed into the mixed solution and transferred into a 50-mL Teflon-lined stainless steel autoclave. After being heated for 16 h at 120 °C, the sealed autoclave naturally cooled down. The substrates were washed with ethanol and deionized water to remove the residual reactants. After being dried for 12 h at 60 °C in a vacuum oven, the obtained precursors were annealed at a slow heating rate of 2 °C/min at 450 °C for 4 h in a nitrogen atmosphere. The neutral sample was synthesized by following the process given above without adding COOH. The corresponding samples were denoted as CoO-NFs (acidity) and CoO-FLs (neutral), respectively.

2.2. Material Characterizations

The chemical constituents of the samples were evaluated by X-ray photoelectron spectroscopy (XPS, Axis Ultra DLD, Kratos, Shimadzu, Japan) and an X-ray diffractometer (XRD, BRUKER D8 ADVANCE, Cu $\text{K}\alpha 1$: 1.5406, Billerica, MA, USA). The morphologies and structures of the synthesized products were determined by scanning electron microscopy (FESEM, 5 kV, ZEISS Ultra 55, Pt-spraying treatment, Oberkochen, Germany) and transmission electron microscopy (TEM, 200 kV, JEM-2100HR, JEOL Ltd., Beijing, China). ICP-OES analysis was evaluated by an inductively coupled plasma-optical emission spectrometer (SPECTRO ARCOS ICP-OES analyzer, SPECTRO, Kleve, Germany). The pore distribution and the specific surface area of the products were characterized by the Brunauer–Emmett–Teller area measurement (BET, Micromeritics ASAP 2020, Micromeritics, Shanghai, China).

2.3. Electrochemical Measurements

Galvanostatic charge/discharge (GC) measurements were performed on the LAND cell test system (Land CT 2001A, Sanland, Wuhan, China) using CR2032-type coin cells. Cyclic voltammetry (CV) measurements and impedance spectra were carried out with an electrochemical workstation (CHI 660E, Chenhua, Shanghai, China) in the frequency range from 0.01 Hz to 10 kHz. For comparison, coin cells were assembled to investigate the electrochemical properties of CoO-NFs and CoO-FLs.

The synthesized CoO-NFs and CoO-FLs, as binder-free anodes, were used directly for electrochemical tests. The counter and reference electrodes were lithium foil, while the separator was polypropylene membrane (Celgard 2400). 1 M LiPF₆ dissolved in a 1:1 (vol.) mixture of diethyl carbonate (DEC) and ethylene carbonate (EC) was used as the electrolyte. An argon-filled glove box (LG1200/750TS, Vigor, Suzhou, China) was used to assemble the CR2032-type coin cells.

3. Results and Discussion

3.1. Structural and Morphological Characterization

To estimate the loading mass of CoO on copper foam, the result of the ICP-OES test is displayed in Table 2. The samples of CoO-NFs and CoO-FLs were prepared using the same process. Therefore, the mass loading of CoO is estimated according to Equation (1) and the average of the results is used for the electrochemical measurements.

$$m_{CoO} = \frac{m_{Co} \times M_{CoO}}{M_{Co}} \quad (1)$$

Table 2. The element mass fraction of CoO-NFs and CoO-FLs.

Samples	Co (mg)	Average (mg)
NF-1	2.256	2.021
NF-2	1.785	
FL-1	1.246	1.161
FL-2	1.076	

The crystalline phases of CoO-NFs and CoO-FLs are confirmed with the XRD patterns (Figure 1). The peaks of CoO-NFs are similar to CoO-FLs. Diffraction peaks located at 36.50°, 42.40°, 61.52°, 73.70°, and 77.56° match very well with the (111), (200), (220), (311), and (222) planes of the standard CoO phase (JCPDS No.43-1004). Moreover, additional diffraction peaks at 43.4°, 50.5°, and 74.3° correspond to the (111), (200), and (220) planes of copper foam (JCPDS No. 65-9743). The characteristic peaks of CoO-NFs are stronger and sharper than CoO-FLs, which manifest better crystallinity and higher crystalline purity than CoO-NFs.

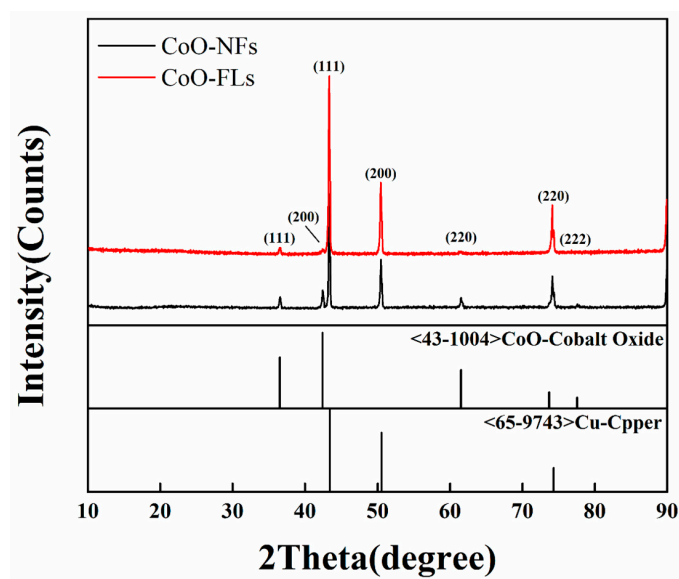


Figure 1. XRD patterns of CoO-NFs and CoO-FLs.

To further confirm the chemical compositions, Figure 2a shows the CoO-NFs detected by X-ray photoelectron measurement. The XPS wide survey spectrum verifies the presence of elemental Cu, Co, and O in CoO-NFs. The Co 2p spectrum is shown in Figure 2b. The peaks at 780.1 eV and 796.4 eV are assigned to Co 2p_{3/2} and Co 2p_{1/2}, respectively. Furthermore, the peaks at 786.1 eV and 802.8 eV are associated with Co 2p_{3/2} and Co 2p_{1/2} shakeup satellite, respectively [36–38]. The Co 2p pattern suggests a divalent cobalt oxidation state, displaying the formation of a Co–O bond in CoO-NFs.

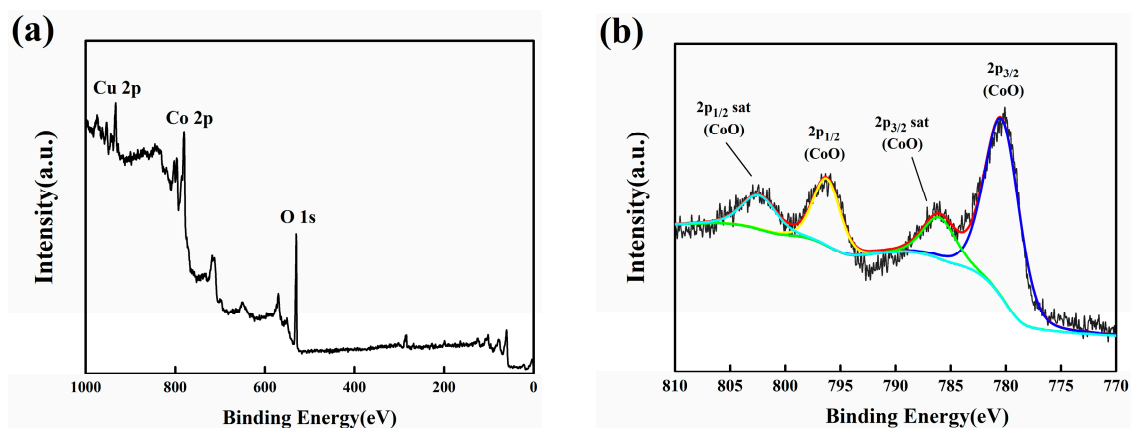


Figure 2. XPS survey spectrum (a) and spectra of Co 2p (b) performed on CoO-NFs.

Next we investigated the morphologies of as-prepared nanosized CoO electrodes. In the low-magnification pattern, as shown in Figure 3a, reticular copper foam covered with many flakes can be observed. The magnified pattern (inserts in Figure 3a) exhibits dozens of nanoflakes uniformly distributed on the substrate; the thickness of the flakes is just a few tens of nanometers. These interlaced nanoflakes have a regular vertical arrangement and offer enough free space and a large surface area, which is beneficial to ion/electron transport. Figure 3b and the inset show the low and high magnification SEM patterns of CoO-FLs. In the low magnification pattern, CoO clusters with a flower-like structure can be observed. The CoO flakes grew not only on the surface, but also suspended over the cavities of copper foam. Without the support of copper foam, the CoO-FLs anode was vulnerable to structural damage during the lithium ion transport process. The morphology and structure of CoO-NFs and CoO-FLs were investigated by transmission electron microscopy in Figure 3c–f. As observed, the morphologies of CoO-NFs and CoO-FLs are in coordination with the SEM images exhibited above. Figure 3c shows that CoO-NFs are composed of numerous interconnected nanoparticles, manifesting porous architecture. This unique configuration can not only conveniently facilitate the infiltration of electrolyte into the electrode but also maintain structural stability. In contrast, CoO-FLs have the characteristic of a smooth and compact surface, shown in Figure 3d, which would impede the immersing of the electrolyte and the diffusion of lithium ions. The high-resolution TEM image of CoO-NFs in Figure 3e shows two kinds of clear and continuous fringes in the same orientation, with lattice spacing of 0.213 and 0.246 nm, which correspond to the (200) and (111) planes of CoO-NFs, respectively. The structure of CoO-NFs was further confirmed by the electron diffraction pattern in the same area, as shown in Figure 3f. The three diffraction rings are ascribed to the (220), (200), and (111) planes [39], which have a mutually verifying relationship with the analysis of XRD pattern (Figure 1).

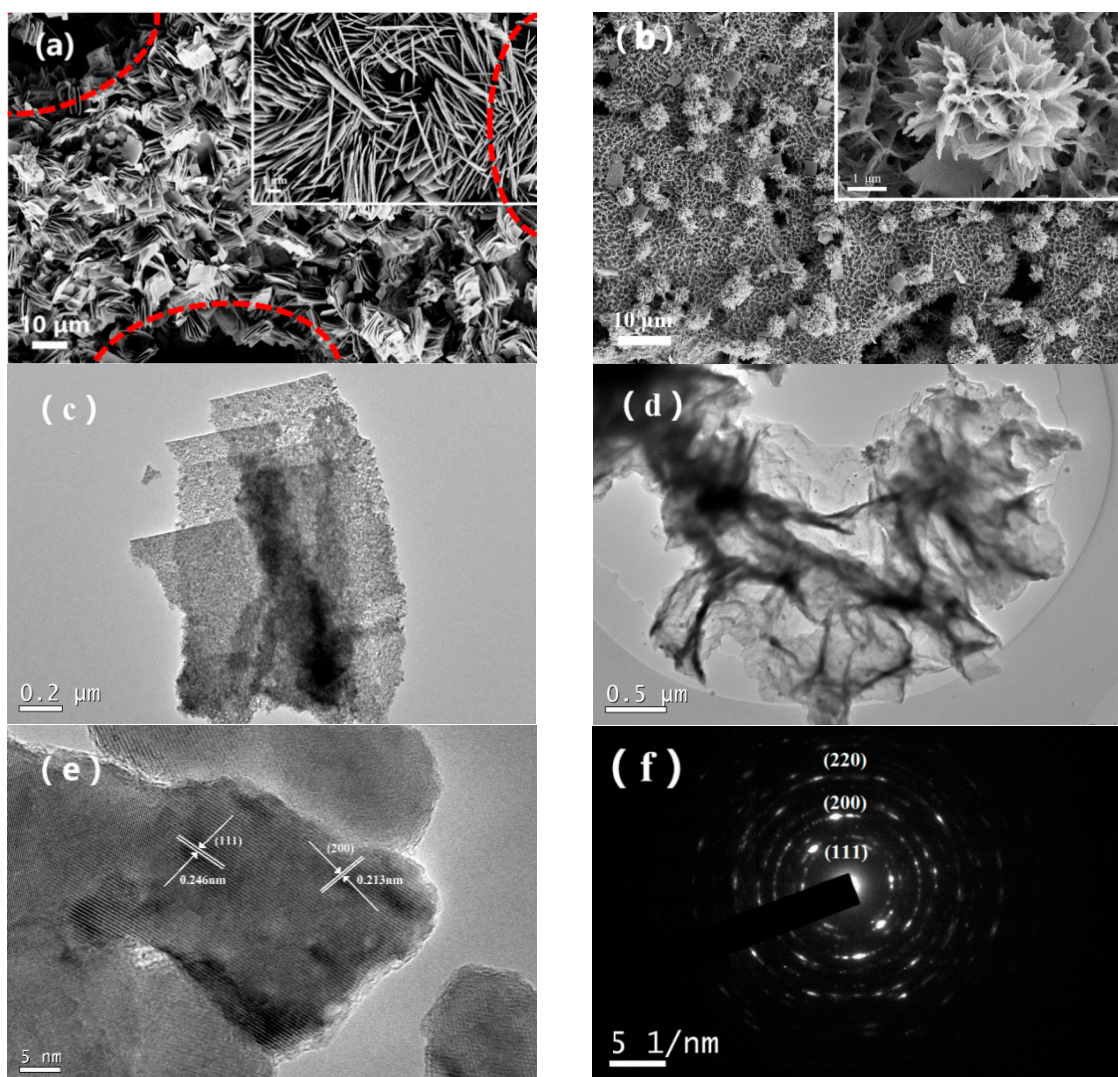


Figure 3. SEM images of CoO-NFs (a) and CoO-FLs (b); TEM images of CoO-NFs (c) and CoO-FLs (d); HRTEM image (e); and the selected area electron diffraction (SAED) pattern (f) of CoO-NFs.

3.2. Electrochemical Performances

To demonstrate the electrochemical performances of CoO-NFs and CoO-FLs, the cyclic voltammetry was carried out in a voltage range of 0.01–3.0 V at a slow scan rate of 0.2 mV s⁻¹ (Figure 4a). Cathodic peaks in the first cycle at ~0.35 V are found in both CoO-NFs and CoO-FLs, corresponding to the formation of the solid electrolyte interface film, while cathodic peaks at 1.0–1.2 V are ascribed to the reduction of CoO into Co [40,41]. In the anodic process, therefore, the oxidation peaks of both CoO-NFs and CoO-FLs that appear at 2.25 V can be associated with the decomposition of Li₂O. In the second cycle, the cathodic peaks shifted to 1.25 V because of the amorphization of CoO and the formation of ultrafine nanograins during the first cycle [42]. Figure 4b exhibits the discharge/charge curves of CoO-NFs at 100 mA g⁻¹ current density. The first discharge profile has a long plateau at about 0.75 V, which is ascribed to the formation of the SEI films and the complex phase transformation of CoO to Co. This electrochemical reaction can be described as in Equation (2). The first charge profile displays a strong polarization at 1.4 V. There is a voltage plateau at 2.25 V, corresponding to Equation (3). Then the plateau shifts to higher voltage at ~1.5 V in the following discharge profiles.





The voltage hysteresis exhibited in the following cycles is a general phenomenon for the transition metal oxide Li-ion batteries' anode materials and could be noted as the signature of the conversion mechanism [43]. The CoO-NFs deliver 1113 mA h g⁻¹ and 1470 mA h g⁻¹ for charge and discharge capacity, respectively. The high surface area of the nanostructure of the anode not only increases the reactive sites of the electrode/electrolyte, but also increases the Li⁺ consumption resulting from the SEI (solid electrolyte interface) formation. Moreover, a series of side reactions at initial cycles such as the reduction of the metal oxide, the decomposition of the electrolyte, and the reaction of the oxygen-containing functional groups on the metal oxide surface with Li⁺ is also responsible for the irreversible capacity [44]. Moreover, the sloped plateaus of discharge at ~0.8 V and ~1.25 V during the following cycles are in coordination with the cyclic voltammetry result.

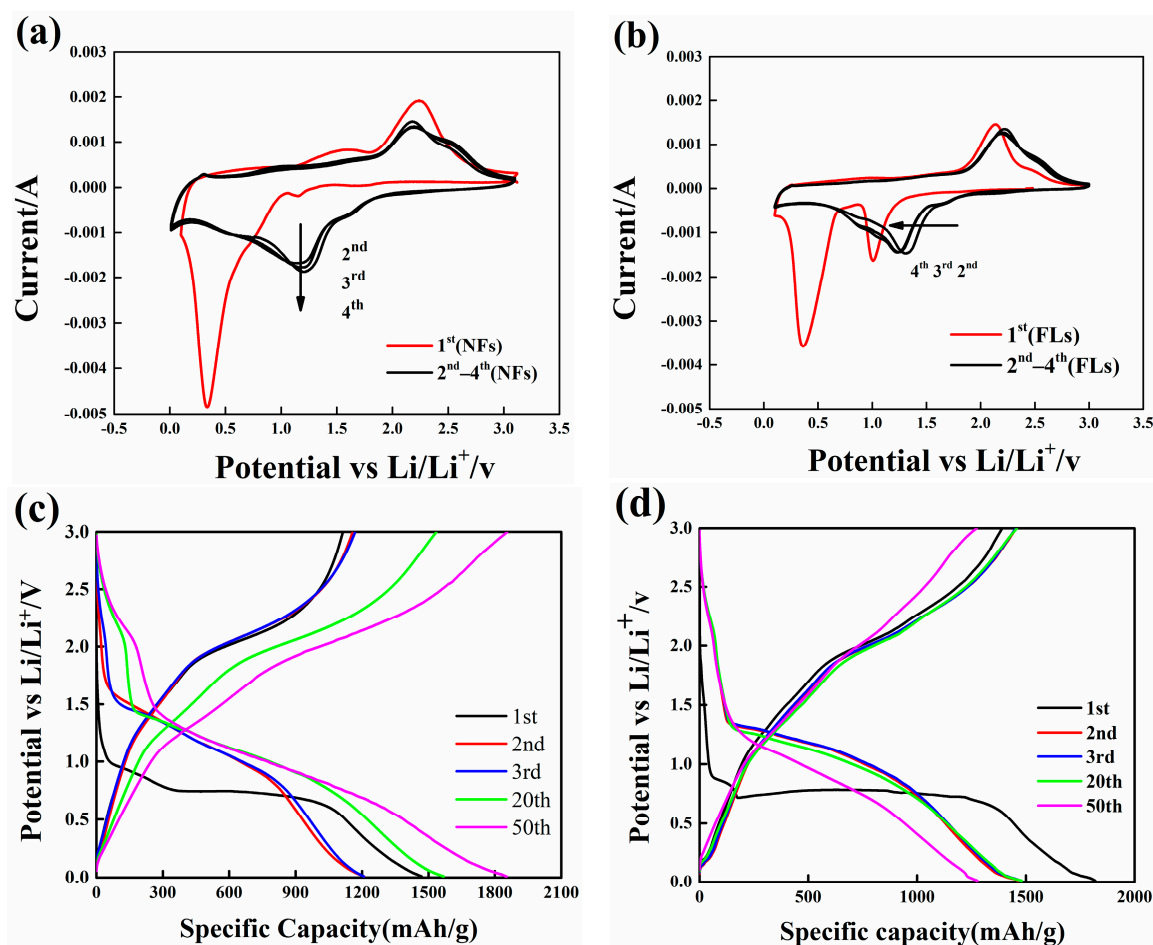


Figure 4. CV curves for the first four cycles of CoO-NFs (a) and CoO-FLs (b) at a scan rate of 0.2 mV s⁻¹; Discharge and charge voltage profiles of the CoO-NFs (c) and CoO-FLs (d) at a current density of 100 mA g⁻¹.

Figure 5a shows the cycling performance of CoO-NFs and CoO-FLs at room temperature at 100 mA g⁻¹ current density. As shown in the picture, CoO-NFs and CoO-FLs exhibit high initial and reversible capacity during 80 cycles. The copper foam, as a current collector, not only extended the electron/electrolyte interface but also promoted the conductivity of the full electrodes. The initial coulombic efficiencies of CoO-NFs and CoO-FLs are 75.7% and 73.4%, respectively. This may result from the large surface area of two samples so that more irreversible Li⁺ was consumed in the formation of SEI films. The coulombic efficiency increases to ~96% (in the second cycle) and the tendency is

upward in the following cycles. Researchers have observed a similar capacity rise phenomenon during cycling in transition-metal oxide composite anode materials [45,46]. The dominant factor in the increase in capacity can be regarded as the reversible growth of polymer/gel-like films [46,47]. In the process of conversion, the polymeric films can be ascribed to kinetically active electrolyte degradation [48]. After 60 cycles, the cycling performance of the two samples gradually becomes stable. The reversible capacity is 1776 mA h g⁻¹ after 80 cycles, which is significant improvement compared with the reported CoO-Ni foam electrode [34]. The rate capability of CoO-NFs and CoO-FLs is tested at a series of rates to estimate their electrochemical performance. As shown in Figure 5b, the average discharge capacities of CoO-NFs are 1459, 1457, 1353, 1038, 868, and 494 mA h g⁻¹ at a current density of 100, 300, 500, 1000, 2000, and 5000 mA g⁻¹ (each for 10 cycles), respectively. For comparison, the CoO-FLs are tested under the same conditions. Their average discharge capacities are 1521, 1361, 1187, 383, and 179 mA h g⁻¹, respectively. After increasing the current density from 100 to 5000 mA g⁻¹ (60 cycles), the average discharge capacities of CoO-NFs and CoO-FLs stay at 1556 mA h g⁻¹ and 1276 mA h g⁻¹ when the current density comes back to 100 mA g⁻¹. Obviously, both CoO-NFs and CoO-FLs manifest a good rate capability. This may be attributed to the following aspect: the copper foam, acting as an elastic support, provides porous features for the growth of the nanosized CoO, which reduces the exchange resistance of Li⁺ between active materials and electrolytes and shortens the charge-transfer pathway [49].

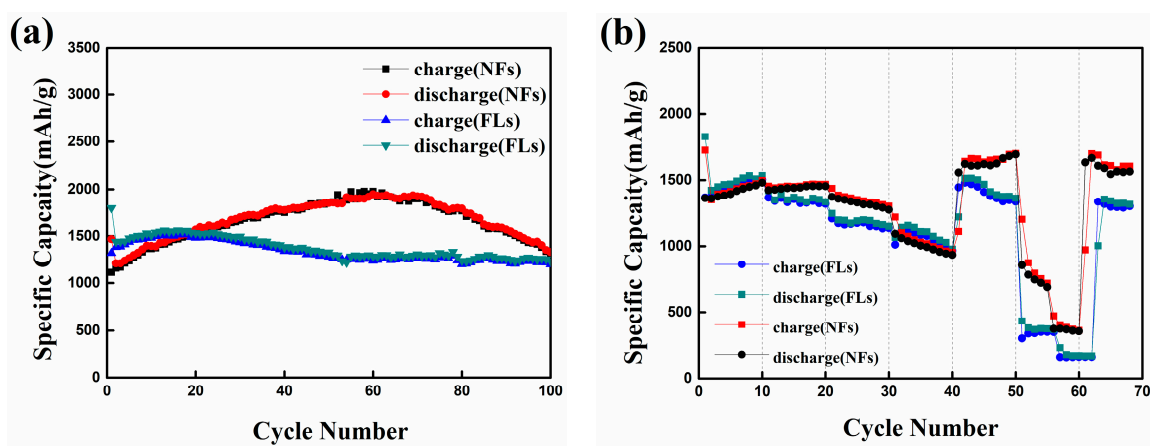


Figure 5. (a) Comparative cycling performance of CoO-NFs and CoO-FLs at 100 mA g⁻¹; (b) the rate capability of CoO-NFs and CoO-FLs at different current densities.

The comparison of impedance plots of CoO-NFs and CoO-FLs is shown in Figure 6a at a frequency range from 0.01 Hz to 10 kHz. The high-frequency area reflects the bulk cell resistance (R_s), which relates to the electrode and the electrolyte. The existence of the semicircle is usually ascribed to the charge transfer process, while R_{ct} is the charge transfer resistance results from the semicircle diameter. Evidently, the diameter of the semicircle for CoO-NFs is much smaller than that for CoO-FLs, indicating lower charge-transfer impedance in the electrode/electrolyte. CPE1 (constant phase element) is a capacitance element coupled with R_{ct} . The inclined line in the low-frequency area indicates the Warburg impedance associated with the lithium-diffusion process (Z_w) [50]. Evidently, the semicircle diameter of the samples in the 80 cycle is correspondingly larger than the samples in the first cycle. This may be ascribed to the structural integrity of the electrodes (displayed in Figure 7a,b) and the thickening of the SEI films when Li⁺ is continuously deposited on the surface [51]. Furthermore, the three-dimensional porous structure of copper foam contributes a large specific surface area of 24.8 m²/g for CoO-NFs and 32.8 m²/g for CoO-FLs, measured by BET, as shown in Figure 6b. The larger specific surface of CoO-FLs causes the formation of more SEI films and irreversible capacity loss, which may be an explanation for the difference in electrochemical performance between CoO-NFs and CoO-FLs.

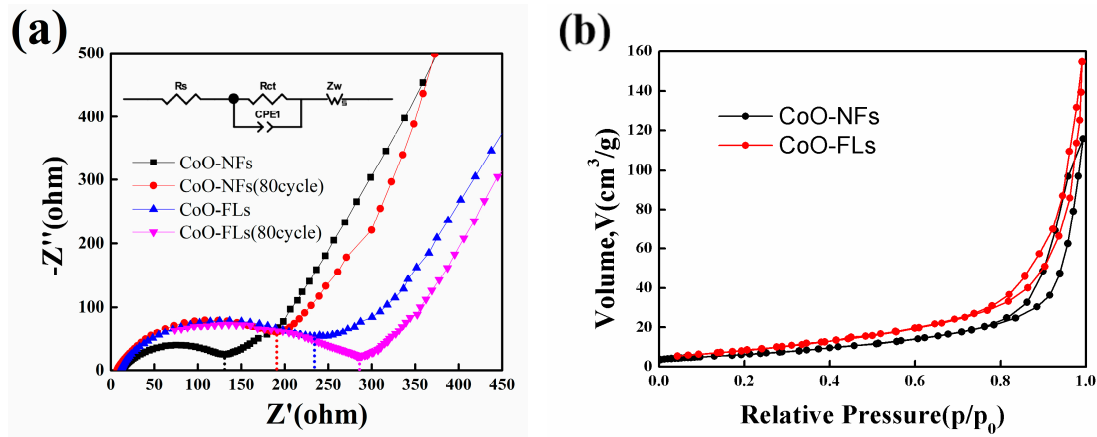


Figure 6. Electrochemical impedance spectra (a) and the N₂ adsorption/desorption isotherms (b) of CoO-NFs and CoO-FLs.

Figure 7a,b shows the morphologies of CoO-NFs and CoO-FLs after 80 cycles. It can be seen from Figure 7a that the nanoflakes are staggered, so the specific structure can be retained. It can be seen in Figure 7b that there are many large cracks over the surface, which indicates the destruction of the CoO-FLs' anode. Furthermore, it can be seen from the XRD patterns (Figure 7c,d) that CoO-NFs shows better crystal perfection than CoO-FLs. The structural damage during the lithium intercalation and deintercalation process is more serious in CoO-FLs, which is consistent with the results of SEM in Figure 7a,b. Compared with CoO-FLs, CoO-NFs exhibit higher reversible capacity and better cycle stability after 80 cycles at the same current densities. This may be attributed to the maintenance of a compact and staggered structure after long-term cycling.

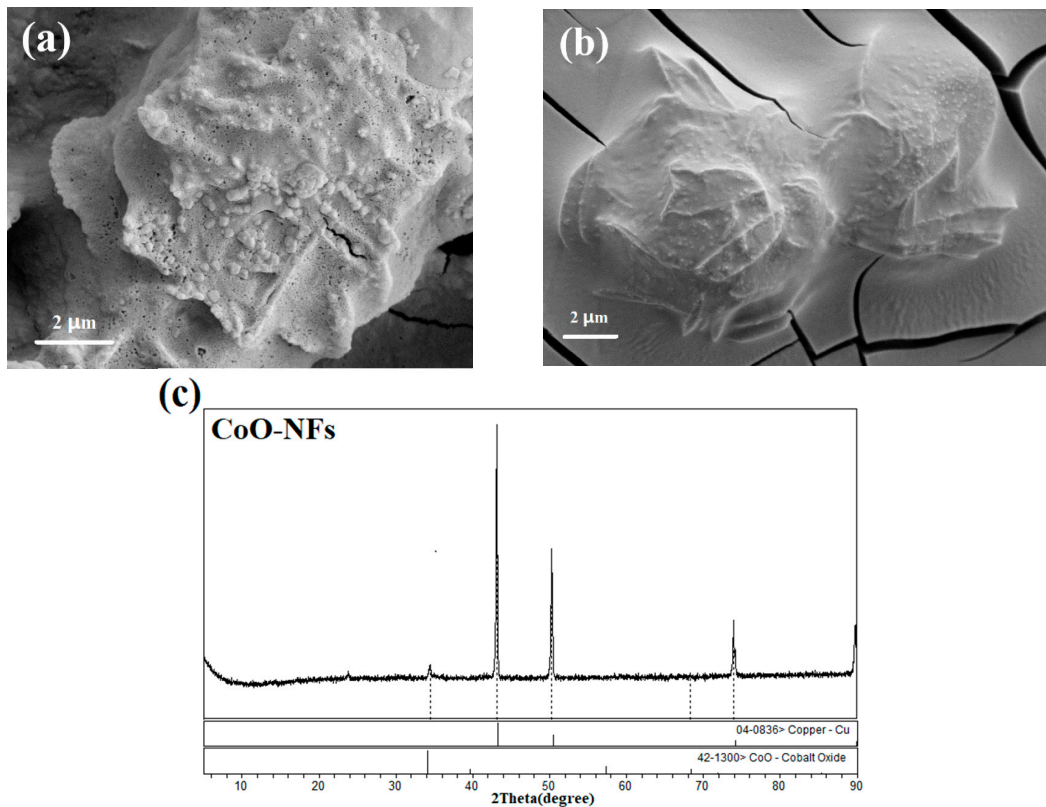


Figure 7. Cont.

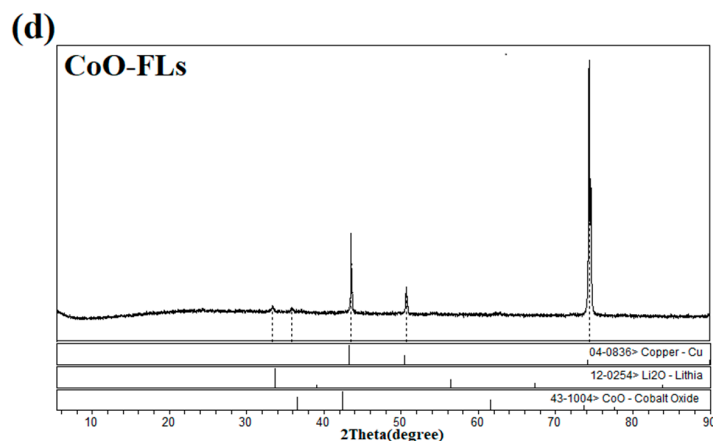


Figure 7. The morphologies and XRD pattern of CoO-NFs electrode (a,c) and CoO-FLs (b,d) after 80 cycles.

4. Conclusions

In summary, two different morphologies of nanosized CoO electrodes are successfully fabricated on a copper foam substrate through the hydrothermal method by adjusting the pH values of solutions. The as-prepared CoO-NFs and CoO-FLs, as anode materials for LIBs, exhibit excellent electrochemical performance. CoO-NFs, in particular, achieved a reversible capacity of 1776 mA h g^{-1} after 80 cycles at 100 mA g^{-1} , proving that they are a promising anode material for high-capacity LIBs. This work also provides new insight into the choosing of different current collectors to fabricate high-quality, binder-free electrodes, which can greatly enhance the performance of LIBs.

Acknowledgments: This work was supported by the Key Projects of Guangdong Province Nature Science Foundation (No. 2017B030311013) and the Scientific and Technological Plan of Guangdong Province, Guangzhou City, and Longhua District of Shenzhen City, China (Nos. 201804010169, 2017B020227009, 2017A040405048, 2017A040405047, 2017A040405049, 2016A040403109, 2016A050502054, 2016A050503019, 20150529A0900008).

Author Contributions: Mingna Liao and Qilun Zhang conceived the experiments and wrote the paper; Youpeng Li and Xin Zhou analyzed the data, Yali Zhang, and Zhiwei Xu performed the experiments; Chenghao Yang and Fengling Tang contributed analysis tools and collect data; Qiang Ru and Lingzhi Zhao guided and supervised the work.

Conflicts of Interest: The authors declare no conflict of interest.

References

1. Etacheri, V.; Marom, R.; Elazari, R.; Salitra, G.; Aurbach, D. Challenges in the development of advanced Li-ion batteries: A review. *Energy Environ. Sci.* **2011**, *4*, 3243. [[CrossRef](#)]
2. Xin, S.; Guo, Y.; Wan, L. Nanocarbon networks for advanced rechargeable lithium batteries, Accounts of chemical research. *Accounts Chem. Res.* **2012**, *45*, 1759–1769. [[CrossRef](#)] [[PubMed](#)]
3. Tang, W.; Zhu, Y.; Hou, Y.; Liu, L.; Wu, Y.; Loh, K.P.; Zhang, H.; Zhu, K. Aqueous rechargeable lithium batteries as an energy storage system of superfast charging. *Energy Environ. Sci.* **2013**, *6*, 2093. [[CrossRef](#)]
4. Amine, K.; Kanno, R.; Tzeng, Y. Rechargeable lithium batteries and beyond: Progress, challenges, and future directions. *MRS Bull.* **2014**, *39*, 395–401. [[CrossRef](#)]
5. Vilatela, J.J.; Eder, D. Nanocarbon composites and hybrids in sustainability: A review. *ChemSusChem* **2012**, *5*, 456–478. [[CrossRef](#)] [[PubMed](#)]
6. Elia, G.A.; Park, J.-B.; Sun, Y.-K.; Scrosati, B.; Hassoun, J. Role of the Lithium Salt in the Performance of Lithium-Oxygen Batteries: A Comparative Study. *ChemElectroChem* **2014**, *1*, 47–50. [[CrossRef](#)]
7. Srivastava, M.; Singh, J.; Kuila, T.; Layek, R.K.; Kim, N.H.; Lee, J.H. Recent advances in graphene and its metal-oxide hybrid nanostructures for lithium-ion batteries. *Nanoscale* **2015**, *7*, 4820–4868. [[CrossRef](#)] [[PubMed](#)]

8. Wang, Z.; Zhou, L.; Lou, X.W.D. Metal Oxide Hollow Nanostructures for Lithium-ion Batteries. *Adv. Mater.* **2012**, *24*, 1903–1911. [[CrossRef](#)] [[PubMed](#)]
9. Tian, Q.; Zhang, W. The lithium storage properties of potassium octatitanate as anode materials for lithium-ion batteries. *Mater. Lett.* **2017**, *190*, 177–180. [[CrossRef](#)]
10. Dhanabalan, A.; Li, X.; Agrawal, R.; Chen, C.; Wang, C. Fabrication and Characterization of SnO(2)/Graphene Composites as High Capacity Anodes for Li-Ion Batteries. *Nanomaterials* **2013**, *3*, 606–614. [[CrossRef](#)] [[PubMed](#)]
11. Kundu, M.; Karunakaran, G.; Kolesnikov, E.; Sergeevna, V.E.; Kumari, S.; Gorshenkov, M.V.; Kuznetsov, D. Hollow NiCo₂O₄ nano-spheres obtained by ultrasonic spray pyrolysis method with wuperior electrochemical performance for lithium-ion batteries and supercapacitors. *J. Ind. Eng. Chem.* **2018**, *59*, 90–98. [[CrossRef](#)]
12. Julien, C.M.; Mauger, A.A. Nanostructured MnO(2) as Electrode Materials for Energy Storage. *Nanomaterials* **2017**, *7*. [[CrossRef](#)]
13. Kundu, M.; Karunakaran, G.; Kolesnikov, E.; Dmitry, A.; Gorshenkov, M.V.; Kuznetsov, D. Hollow (Co_{0.6}2Fe_{1.38})FeO₄/NiCo₂O₄ nanoboxes with porous shell synthesized via chemical precipitation: A novel form as a high performance lithium ion battery anode. *Microporous Mesoporous Mater.* **2017**, *247*, 9–15. [[CrossRef](#)]
14. Iturrondobeitia, A.; Goni, A.; Gil de Muro, I.; Lezama, L.; Rojo, T. Physico-Chemical and Electrochemical Properties of Nanoparticulate NiO/C Composites for High Performance Lithium and Sodium Ion Battery Anodes. *Nanomaterials* **2017**, *7*. [[CrossRef](#)] [[PubMed](#)]
15. Ji, L.; Lin, Z.; Alcoutlabi, M.; Zhang, X. Recent developments in nanostructured anode materials for rechargeable lithium-ion batteries. *Energy Environ. Sci.* **2011**, *4*, 2682. [[CrossRef](#)]
16. Zhang, Y.; Wu, Y.; Chu, Y.; Li, L.; Yu, Q.; Zhu, Y.; Liu, G.; Hou, Q.; Zeng, R.; Zhao, L. Self-assembled Co₃O₄ nanostructure with controllable morphology towards high performance anode for lithium ion batteries. *Electrochim. Acta* **2016**, *188*, 909–916. [[CrossRef](#)]
17. Chen, C.; Huang, Y.; Zhang, H.; Wang, X.; Wang, Y.; Jiao, L.; Yuan, H. Controllable synthesis of Cu-doped CoO hierarchical structure for high performance lithium-ion battery, *Journal of Power Sources. J. Power Sources* **2016**, *314*, 66–75. [[CrossRef](#)]
18. Xue, X.Y.; Yuan, S.; Xing, L.L.; Chen, Z.H.; He, B.; Chen, Y.J. Porous Co₃O₄ nanoneedle arrays growing directly on copper foils and their ultrafast charging/discharging as lithium-ion battery anodes. *Chem. Commun.* **2011**, *47*, 4718–4720. [[CrossRef](#)] [[PubMed](#)]
19. Du, N.; Zhang, H.; Chen, B.D.; Wu, J.B.; Ma, X.Y.; Liu, Z.H.; Zhang, Y.Q.; Yang, D.R.; Huang, X.H.; Tu, J.P. Porous Co₃O₄ Nanotubes Derived From Co₄(CO)₁₂ Clusters on Carbon Nanotube Templates: A Highly Efficient Material For Li-Battery Applications. *Adv. Mater.* **2007**, *19*, 4505–4509. [[CrossRef](#)]
20. Liu, J.; Xia, H.; Lu, L.; Xue, D. Anisotropic Co₃O₄ porous nanocapsules toward high-capacity Li-ion batteries. *J. Mater. Chem.* **2010**, *20*, 1506. [[CrossRef](#)]
21. Wang, J.; Yang, N.; Tang, H.; Dong, Z.; Jin, Q.; Yang, M.; Kisailus, D.; Zhao, H.; Tang, Z.; Wang, D. Accurate control of multishelled Co₃O₄ hollow microspheres as high-performance anode materials in lithium-ion batteries. *Angew. Chem.* **2013**, *52*, 6417–6420. [[CrossRef](#)] [[PubMed](#)]
22. Jiang, J.; Li, Y.; Liu, J.; Huang, X.; Yuan, C.; Lou, X.W. Recent advances in metal oxide-based electrode architecture design for electrochemical energy storage. *Adv. Mater.* **2012**, *24*, 5166–5180. [[CrossRef](#)] [[PubMed](#)]
23. Li, Y.; Shang, K.; Zhou, W.; Tan, L.; Pan, X.; Liao, M.; Lei, J.; Zhao, L. Honeycomb-Spherical Co₃O₄-TiO₂ Hybrid Materials for Enhanced Lithium Storage. *Electrochim. Acta* **2016**, *222*, 1642–1649. [[CrossRef](#)]
24. Guan, X.; Nai, J.; Zhang, Y.; Wang, P.; Yang, J.; Zheng, L.; Zhang, J.; Guo, L. CoO Hollow Cube/Reduced Graphene Oxide Composites with Enhanced Lithium Storage Capability. *Chem. Mater.* **2014**, *26*, 5958–5964. [[CrossRef](#)]
25. Leng, X.; Ding, X.; Hu, J.; Wei, S.; Jiang, Z.; Lian, J.; Wang, G.; Jiang, Q.; Liu, J. In situ prepared reduced graphene oxide/CoO nanowires mutually-supporting porous structure with enhanced lithium storage performance. *Electrochim. Acta* **2016**, *190*, 276–284. [[CrossRef](#)]
26. Sun, Y.; Hu, X.; Luo, W.; Huang, Y. Ultrathin CoO/Graphene Hybrid Nanosheets: A Highly Stable Anode Material for Lithium-Ion Batteries. *J. Phys. Chem. C* **2012**, *116*, 20794–20799. [[CrossRef](#)]
27. Yang, Y.; Ji, X.; Jing, M.; Hou, H.; Zhu, Y.; Fang, L.; Yang, X.; Chen, Q.; Banks, C.E. Carbon dots supported upon N-doped TiO₂nanorods applied into sodium and lithium ion batteries. *J. Mater. Chem. A* **2015**, *3*, 5648–5655. [[CrossRef](#)]

28. Yao, Y.; Zhu, Y.; Shen, J.; Yang, X.; Li, C. CoO nanosheets derived from electrodeposited cobalt metal towards high performance lithium ion batteries. *Electrochim. Acta* **2016**, *222*, 1300–1307. [[CrossRef](#)]
29. Yuan, W.; Zhao, M.; Yuan, J.; Li, C.M. Ni foam supported three-dimensional vertically aligned and networked layered CoO nanosheet/graphene hybrid array as a high-performance oxygen evolution electrode. *J. Power Sources* **2016**, *319*, 159–167. [[CrossRef](#)]
30. Jiang, J.; Liu, J.; Ding, R.; Ji, X.; Hu, Y.; Li, X.; Hu, A.; Wu, F.; Zhu, Z.; Huang, X. Direct Synthesis of CoO Porous Nanowire Arrays on Ti Substrate and Their Application as Lithium-Ion Battery Electrodes. *J. Phys. Chem. C* **2010**, *114*, 929–932. [[CrossRef](#)]
31. Zhao, S.; Guo, J.; Jiang, F.; Su, Q.; Zhang, J.; Du, G. Growth of hierarchical porous CoO nanowire arrays on carbon cloth as binder-free anodes for high-performance flexible lithium-ion batteries. *J. Alloys Compd.* **2016**, *655*, 372–377. [[CrossRef](#)]
32. Huang, X.; Wang, R.; Xu, D.; Wang, Z.; Wang, H.; Xu, J.; Wu, Z.; Liu, Q.; Zhang, Y.; Zhang, X. Homogeneous CoO on Graphene for Binder-Free and Ultralong-Life Lithium Ion Batteries. *Adv. Funct. Mater.* **2013**, *23*, 4345–4353. [[CrossRef](#)]
33. Cao, K.; Jiao, L.; Liu, Y.; Liu, H.; Wang, Y.; Yuan, H. Ultra-High Capacity Lithium-Ion Batteries with Hierarchical CoO Nanowire Clusters as Binder Free Electrodes. *Adv. Funct. Mater.* **2015**, *25*, 1082–1089. [[CrossRef](#)]
34. Li, D.; Ding, L.-X.; Wang, S.; Cai, D.; Wang, H. Ultrathin and highly-ordered CoO nanosheet arrays for lithium-ion batteries with high cycle stability and rate capability. *J. Mater. Chem. A* **2014**, *2*, 5625–5630. [[CrossRef](#)]
35. Chen, M.; Xia, X.; Qi, M.; Yuan, J.; Yin, J.; Chen, Q. Self-supported porous CoO semisphere arrays as binder-free electrodes for high-performance lithium ion batteries. *Mater. Res. Bull.* **2016**, *73*, 125–129. [[CrossRef](#)]
36. Stevens, G.C.; Edmonds, T. Catalytic activity of the basal and edge planes of molybdenum disulphide, Journal of the Less-Common Metals. *J. Less-Common Met.* **1977**, *54*, 321–330. [[CrossRef](#)]
37. Zhang, P.; Wang, R.; He, M.; Lang, J.; Xu, S.; Yan, X. 3D Hierarchical Co/CoO-Graphene-Carbonized Melamine Foam as a Superior Cathode toward Long-Life Lithium Oxygen Batteries. *Adv. Funct. Mater.* **2016**, *26*, 1354–1364. [[CrossRef](#)]
38. Vempati, S.; Shetty, A.; Dawson, P.; Nanda, K.K.; Krupanidhi, S.B. Solution-based synthesis of cobalt-doped ZnO thin films. *Thin Solid Films* **2012**, *524*, 137–143. [[CrossRef](#)]
39. Qi, Y.; Zhang, H.; Du, N.; Yang, D. Highly loaded CoO/graphene nanocomposites as lithium-ion anodes with superior reversible capacity. *J. Mater. Chem. A* **2013**, *1*, 2337. [[CrossRef](#)]
40. Poizot, P.; Laruelle, S.; Grugeon, S.; Dupont, L.; Tarascon, J.M. Nano-sized transition-metal oxides as negative-electrode materials for lithium-ion batteries. *Nature* **2000**, *407*, 496–499. [[CrossRef](#)] [[PubMed](#)]
41. Huang, X.; Wu, J.; Guo, R.; Lin, Y.; Zhang, P. Aligned nickel-cobalt oxide nanosheet arrays for lithium ion battery applications. *Int. J. Hydrogen Energy* **2014**, *39*, 21399–21404. [[CrossRef](#)]
42. Qin, Y.; Li, Q.; Xu, J.; Wang, X.; Zhao, G.; Liu, C.; Yan, X.; Long, Y.; Yan, S.; Li, S. CoO-Co nanocomposite anode with enhanced electrochemical performance for lithium-ion batteries. *Electrochim. Acta* **2017**, *224*, 90–95. [[CrossRef](#)]
43. Wang, Y.; Xia, H.; Lu, L.; Lin, J. Excellent Performance in Lithium-Ion Battery Anodes: Rational Synthesis of $\text{Co}(\text{CO}_3)_{0.5}(\text{OH})_{0.11}\text{H}_2\text{O}$ Nanobelt Array and Its Conversion into Mesoporous and Single-Crystal Co_3O_4 . *ACS Nano* **2010**, *4*, 1425–1432. [[CrossRef](#)] [[PubMed](#)]
44. Agubra, V.A.; Zuniga, L.; Flores, D.; Campos, H.; Villarreal, J.; Alcoutlabi, M. A comparative study on the performance of binary $\text{SnO}_2/\text{NiO}/\text{C}$ and Sn/C composite nanofibers as alternative anode materials for lithium ion batteries. *Electrochim. Acta* **2017**, *224*, 608–621. [[CrossRef](#)]
45. Zhan, L.; Wang, S.; Ding, L.-X.; Li, Z.; Wang, H. Binder-free Co-CoOx nanowire arrays for lithium ion batteries with excellent rate capability and ultra-long cycle life. *J. Mater. Chem. A* **2015**, *3*, 19711–19717. [[CrossRef](#)]
46. Ponrouch, A.; Taberna, P.-L.; Simon, P.; Palacín, M.R. On the origin of the extra capacity at low potential in materials for Li batteries reacting through conversion reaction. *Electrochim. Acta* **2012**, *61*, 13–18. [[CrossRef](#)]
47. Hu, Y.Y.; Liu, Z.; Nam, K.W.; Borkiewicz, O.J.; Cheng, J.; Hua, X.; Dunstan, M.T.; Yu, X.; Wiaderek, K.M.; Du, L.S.; et al. Origin of additional capacities in metal oxide lithium-ion battery electrodes. *Nat. Mater.* **2013**, *12*, 1130–1136. [[CrossRef](#)] [[PubMed](#)]

48. Laruelle, S.; Grugeon, S.; Poizot, P.; Dollé, M.; Dupont, L.; Tarascon, J.M. On the Origin of the Extra Electrochemical Capacity Displayed by MO/Li Cells at Low Potential. *J. Electrochem. Soc.* **2002**, *149*, A627. [[CrossRef](#)]
49. Jing, S.; Jiang, H.; Hu, Y.; Li, C. Directly grown Si nanowire arrays on Cu foam with a coral-like surface for lithium-ion batteries. *Nanoscale* **2014**, *6*, 14441–14445. [[CrossRef](#)] [[PubMed](#)]
50. Zhang, S.S.; Xu, K.; Jow, T.R. Electrochemical impedance study on the low temperature of Li-ion batteries. *Electrochim. Acta* **2004**, *49*, 1057–1061. [[CrossRef](#)]
51. Xu, G.B.; Yang, L.W.; Wei, X.L.; Ding, J.W.; Zhong, J.X.; Chu, P.K. Highly-crystalline ultrathin gadolinium doped and carbon-coated $\text{Li}_4\text{Ti}_5\text{O}_{12}$ nanosheets for enhanced lithium storage. *J. Power Sources* **2015**, *295*, 305–313. [[CrossRef](#)]



© 2018 by the authors. Licensee MDPI, Basel, Switzerland. This article is an open access article distributed under the terms and conditions of the Creative Commons Attribution (CC BY) license (<http://creativecommons.org/licenses/by/4.0/>).